Thermoelectric properties of the unfilled skutterudite $FeSb_3$ from first principles and Seebeck local probes

Sébastien Lemal,[1] Ngoc Nguyen,[2] Johannes de Boor,[3] Philippe Ghosez,[1] Julien Varignon,[1] Benedikt Klobes,[4] Raphaël P. Hermann,[4,5,6] and Matthieu J. Verstraete[7,8]

[1]*Physique Théorique des Matériaux (PhyTheMa), Département de Physique, Université de Liège (B5), B-4000 Liège, Belgium*
[2]*Department of Chemistry and Materials Science Institute, University of Oregon, Eugene, Oregon 97403, USA*
[3]*Institute of Materials Research, German Aerospace Center, Linder Höhe, 51147 Köln, Germany*
[4]*Jülich Centre for Neutron Science JCNS and Peter Grünberg Institut PGI, JARA-FIT, Forschungszentrum Jülich GmbH, D-52425 Jülich, Germany*
[5]*Faculté des Sciences, Université de Liège, B-4000 Liège, Belgium*
[6]*Materials Science and Technology Division, Oak Ridge National Laboratory, Oak Ridge, Tennessee 37831, USA*
[7]*Physique des matériaux et nanostructures (NanoMat), Département de Physique, Université de Liège (B5), B-4000 Liège, Belgium*
[8]*European Theoretical Spectroscopy Facility http://www.etsf.eu*

(Received 12 June 2015; revised manuscript received 28 August 2015; published 16 November 2015)

Using a combination of first-principles calculations and experimental transport measurements, we study the electronic and magnetic structure of the unfilled skutterudite $FeSb_3$. We employ the hybrid functional approach for exchange correlation. The ground state is determined to be antiferromagnetic with an atomic magnetic moment of 1.6 μ_B/Fe. The Néel temperature T_N is estimated at 6 K, in agreement with experiments which found a paramagnetic state down to 10 K. The ground state is semiconducting, with a small electronic gap of 33 meV, also consistent with previous experiments on films. Charge carrier concentrations are estimated from Hall resistance measurements. The Seebeck coefficient is measured and mapped using a scanning probe at room temperature that yields an average value of 38.6 μV K^{-1}, slightly lower than the theoretical result. The theoretical conductivity is analyzed as a function of temperature and concentration of charge carriers.

DOI: 10.1103/PhysRevB.92.205204 PACS number(s): 31.15.A−, 85.80.Fi, 84.60.Rb

I. INTRODUCTION

In the context of energy and environmental issues that have become critical in the 21st century, there has been recent increase of interest in thermoelectric (TE) materials, which have the property to convert waste heat into electricity. The efficiency of a thermoelectric device is quantified by the adimensional thermoelectric figure of merit,

$$ZT = \frac{S^2\sigma}{\kappa_e + \kappa_l} T, \tag{1}$$

where S is the Seebeck coefficient, σ is the electrical conductivity, κ_e is the electronic contribution to the thermal conductivity, and κ_l is the lattice contribution to the thermal conductivity. T is the absolute temperature. Optimizing the figure of merit consists of (a) increasing the Seebeck coefficient, which is the ratio between the electric field and the temperature gradient across the compound, (b) increasing the electrical conductivity in order to lower the Ohmic loss in electrical energy, while (c) reducing the thermal conductivity, which is detrimental to the temperature gradient. However, all these properties are usually linked to the electronic properties, and in most cases, it is difficult to optimize all three of them simultaneously.

With this in mind, interest started to gather in the early 1990s around skutterudite compounds, both filled and unfilled. These have been intensively studied over the past two decades, as they display large Seebeck coefficients, and low thermal conductivities which are mainly attributed to phonon scattering by the filler atoms. The most heavily studied compound of this family is $CoSb_3$, which can be filled as RCo_4Sb_{12} with monovalent ions (e.g., $R = Na^+$), divalent ions, or even trivalent ions. The $CoSb_3$ does not accommodate high degrees of filling, but this limitation can be overcome by substituting the Co atoms by Fe atoms. The full substitution results in unfilled $FeSb_3$, our compound of interest. While $FeSb_3$ has not yet been synthesized in bulk, thick films have been grown and studied [2–4]. Experiments suggest a semiconducting compound with a small gap, which is paramagnetic at least down to 10 K. There are some variations in the lattice constant between studies, and also carrier densities as we will show below.

Theoretical studies of bulk $FeSb_3$ have been performed by Råsander *et al.*, using DFT in the generalized gradient approximation, with the projector augmented wave method [5]. They find a ferromagnetic ground state and also study phonons and filler atoms. These results have been confirmed by Xing *et al.* [6], finding a ferromagnetic ground state with LSDA and PBE functionals. These results will serve as a basis for comparison with our theoretical study of bulk $FeSb_3$ and the study of the thermoelectric properties.

Additional DFT studies, along with synthesis and characterization of $FeSb_3$ films, were performed by Daniel *et al.* [4]. Their results are quite different from previous studies. For instance, their films have metallic conductivities, high carrier concentrations, and all of their (nonmagnetic) DFT calculations result in metallic ground states, in contrast to the "half-semiconducting" ground state of Råsander *et al.* [5].

In the present paper, we clarify the properties of unfilled $FeSb_3$. The structural, magnetic, electronic, and thermoelectric properties will be explored, using a combination of first-principles calculations, Hall effect measurements, and Seebeck local probe experiments.

II. METHODS

A. Computational details

We compute the structural, electronic, and magnetic properties of $FeSb_3$ within the density functional theory (DFT). We use the CRYSTAL code [7], which implements the linear combination of atomic orbitals (LCAO) method and the Kohn-Sham ansatz [8] to describe the electronic system of bulk $FeSb_3$ with a local Gaussian basis set. Different basis sets for Fe and Sb atoms were tested, and we selected the ones from Refs. [9,10]. The exchange-correlation energy is modeled within the local density approximation, with the LDA [11] and the B1WC hybrid functional [12], which uses the Becke GGA functional for the exchange energy [13] and the Wu-Cohen [14] GGA functional for the correlation energy. With this hybrid functional, we aim to correctly reproduce the magnetic ground state and confirm the presence of a band gap in $FeSb_3$, by taking 16% of the Hartree-Fock (HF) exchange energy E_x^0. We also relax the structure with the B3LYP [15] hybrid functional, which takes 20% of the real exchange energy, for comparison. The B1WC was designed to reproduce correctly properties of oxides, specifically perovskite $BaTiO_3$ and $PbTiO_3$. Until then, semilocal functionals and standard hybrids could not predict both the electronic and structural properties of these compounds. The performance of hybrid functionals has been reviewed in Refs. [16,17], with the conclusion that it is an ideal formalism to get past the typical shortcomings of semilocal functionals. Numerous papers have been published, based on the B1WC functional in several fields of physics, such has ferroelectrics [12,18], ferromagnets [19], bidimensional electron gas at oxide interfaces [20], or thermoelectrics [21,22]. The B1WC hybrid has demonstrated its ability to model magnetic systems, and has the advantage of being parameter free. This motivated the use of the B1WC functional for predicting the properties of $FeSb_3$.

Three different phases are computed: a non-spin-polarized phase (NM), a ferromagnetic phase between first-neighbor Fe atoms (FM), and an antiferromagnetic phase between first-neighbor Fe atoms (AFM-G). For the AFM-G phase, the space group has been changed from cubic $Im\bar{3}$ to cubic $P23$ to allow the antiferromagnetic order in our simulation. The FM phase was also computed in the $P23$ space group as a test. An $8 \times 8 \times 8$ Monkhorst-Pack [23] k mesh is used for the relaxation of the structure from the room temperature experimental [3] cell parameters ($a_{exp} = 9.1763$ Å) and atomic positions (Table I). The total energy criterion for the self-consistent resolution of the Kohn-Sham problem is fixed to 10^{-8} hartrees.

For each magnetic arrangement, we relax the atomic structure of our compound, and we compare at the total energy for the different phases. As the calculations performed in the $P23$ space group have twice as many atoms as the primitive cells (2×16 atoms), we report the total energy per formula unit. The results in terms of total energy are summarized in Table I.

After relaxing the geometry, the electronic density is calculated on a $16 \times 16 \times 16$ Monkhorst-Pack k mesh. The energy criterion is kept the same. The transport and thermoelectric properties are calculated from the ground state electronic band structure within the Boltzmann transport theory, using the constant relaxation time approximation. The electronic band structure is computed non-self-consistently with a dense uniform $53 \times 53 \times 53$ k mesh with 6579 k points in the irreducible Brillouin zone. With the resulting first-principles band energies, $\epsilon_{i\mathbf{k}}$, we use the BoltzTraP code [24] to estimate the Seebeck coefficient and the electrical conductivity. After performing the Fourier expansion of the band structure, the conductivity tensor $\sigma_{\alpha\beta}(i,\mathbf{k})$ is calculated as

$$\sigma_{\alpha\beta}(i,\mathbf{k}) = e^2 \tau_{i,\mathbf{k}} v_\alpha(i,\mathbf{k}) v_\beta(i,\mathbf{k}), \tag{2}$$

where e is the electronic charge, $\tau_{i,k}$ is the relaxation time, which will be considered independently of i and $\mathbf{k}$ from now on, and $v_\alpha(i,\mathbf{k})$ is the α component of the group velocity for an electron in band i. This quantity is expressed as

$$v_\alpha(i,\mathbf{k}) = \frac{1}{\hbar} \frac{\partial \epsilon_{i,\mathbf{k}}}{\partial k_\alpha}. \tag{3}$$

The spectral conductivity tensor $\sigma_{\alpha\beta}$ can be written as a function of energy:

$$\sigma_{\alpha\beta}(\epsilon) = \frac{1}{8\pi^3} \sum_{i,\mathbf{k}} \delta(\epsilon - \epsilon_{i,\mathbf{k}}) \sigma_{\alpha\beta}(i,\mathbf{k}). \tag{4}$$

In addition to the constant relaxation time approximation, an implicit approximation is the "rigid-band approach": we assume that the band structure does not vary with temperature or doping. The spectral conductivity is then used to calculate the tensors of interest.

If an external electric field or a temperature gradient is applied, we can calculate the transport properties related to the electrical current. The habitual conductivity tensor is

$$\sigma_{\alpha\beta}(T,\mu) = \int -\frac{\partial f(T,\mu)}{\partial \epsilon} \sigma_{\alpha\beta}(\epsilon) d\epsilon. \tag{5}$$

TABLE I. Experimental and optimized cell parameters, fractional coordinates of Sb ions, and total energies (per f.u.) of relaxed $FeSb_3$ for different magnetic phases. The NM phase was chosen as the reference. The asterisk * refers to calculations performed within the $P23$ space group.

Source	Magn.	a (Å)	y	z	ΔE (meV)
Expt. [3] (300 K)		9.1763	0.3400	0.1618	
Expt. [2] (300 K)		9.2384	0.3399	0.1573	
Expt. [4] (300 K)		9.154	0.334	0.158	
This B1WC	NM	8.8958	0.3259	0.1602	0
	FM	8.9788	0.3365	0.1585	−478
	FM*	8.9696	0.3363	0.1584	−478
	AFM-G*	8.9906	0.3369	0.1584	−480
This B3LYP	NM	9.0641	0.3275	0.1574	0
	FM	9.1571	0.3387	0.1560	−852
	AFM-G*	9.1907	0.3398	0.1556	−910
PBE [5]	NM	9.153	0.327	0.160	0
	FM	9.178	0.331	0.160	−280
	AFM	9.166	0.331	0.159	−130
PBE [4]	NM	9.151	0.337	0.161	
	FM	9.167	0.337	0.161	
PW91 [4]	NM	9.153	0.337	0.160	
	FM	9.174	0.341	0.160	
LDA [4]	NM	8.947	0.337	0.160	
	FM	8.943	0.337	0.161	

We also define the following tensor:

$$\nu_{\alpha\beta}(T,\mu) = \frac{1}{eT}\int -\frac{\partial f(T,\mu)}{\partial \epsilon}\sigma_{\alpha\beta}(\epsilon)[\epsilon-\mu]d\epsilon. \quad (6)$$

Equation (6) is used to compute the Seebeck coefficient as

$$S_{ij}(T,\mu) = \sum_{\alpha}(\sigma^{-1})_{\alpha i}(T,\mu)\nu_{\alpha j}(T,\mu). \quad (7)$$

These tensors depend on the temperature T and the chemical potential μ which determines the number of charge carriers. In Eqs. (5) and (6), $f(T,\mu)$ is the Fermi-Dirac distribution. The Hall resistance tensor R_H can also be computed from BoltzTraP [24].

Obtaining a good estimation of the relaxation time is not an easy task considering our aforementioned approximation. More details on the method to estimate τ are given in Sec. III. With this estimated relaxation time, we analyze the behavior of the electrical conductivity σ, as well as the power factor $S^2\sigma$.

B. Experimental methods

The investigated samples are the same as in Ref. [2]. The Seebeck coefficient of a $FeSb_3$ film with a thickness of 1.5 μm was determined at room temperature using a Seebeck microprobe [25,26]. The spatial resolution of the microprobe is of the order of tens of micrometers. This microprobe technique underestimates the absolute value of the Seebeck coefficient, with an error usually between 5%–10%, depending on sample properties. The charge carrier density was determined from Hall effect measurements in van der Pauw geometry [27] using a cryogen-free measurement system (Cryogenic Limited). Within the parabolic band model, the charge carrier density n was calculated from the Hall coefficient R_H using $n_h = \frac{1}{(eR_H)}$, where e is the electron charge.

III. RESULTS AND DISCUSSION

A. Structural properties and magnetism

Unfilled bulk $FeSb_3$ consists of corner-sharing antimony octahedra coordinating iron, as shown in Fig. 1, which displays the conventional cell, in the space group $Im\bar{3}$, where the Fe and the Sb occupy respectively the 8c ($\frac{1}{4}$, $\frac{1}{4}$, $\frac{1}{4}$) and 24g

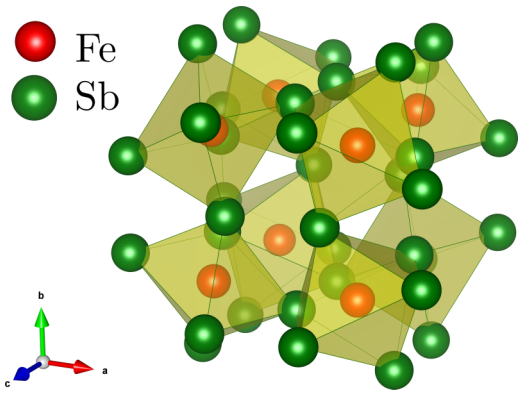

FIG. 1. (Color online) Unfilled skutterudite $FeSb_3$ featuring the corner-sharing $FeSb_6$ octahedra [1].

(0, y, z) Wyckoff positions. The experimental cell parameter and atomic positions are given in Table I. When present, filler ions occupy the positions (0,0,0) and ($\frac{1}{2}$,$\frac{1}{2}$,$\frac{1}{2}$); in other words, the filler ions can occupy the empty space between the $FeSb_6$ octahedra.

We observe that the non-spin-polarized NM case yields the highest total energy, whereas the spin-polarized AFM-G case is the one yielding the lowest total energy, with a significant difference of 480 meV/f.u. Moreover, the difference in energy between the AFM-G case and FM case is only 2 meV, which suggests an easy transition to a paramagnetic phase. This result is in good agreement with the experimental observation of a paramagnetic phase above 10 or 20 K in the case of thin films [2], but in disagreement with previous DFT studies of Råsander *et al.* [5]. They report total energy differences with respect to the nonmagnetic case of −0.28 eV for the FM case, and −0.13 eV for the AFM-G case. In their case, the FM phase is the most stable, and the energy difference between the FM phase and the AFM-G phase is 0.15 eV, which is 75 times larger than our result with the B1WC functional. Our results are in agreement with the experimental picture provided by Möchel *et al.* [2], suggesting that the hybrid functional B1WC provides a better description of the electronic and magnetic structure of $FeSb_3$ than the GGA method. Results obtained with the B3LYP functional are consistent with the B1WC, with a larger energy gap between each magnetic phase. The AFM-G phase remains the most stable one.

The relaxed cell parameter and ionic positions were examined for each simulation. For B1WC, the AFM-G phase yields the lowest difference in the cell parameters and the ionic positions with respect to experimental data, underestimating by 2%. The PBE lattice constants in Refs. [4,5] are larger and close to the experiments in Ref. [4]. The iron keep their initial positions, whereas the antimony atoms move slightly along the y and z directions. The magnetic order has a perceptible effect on the structure: the NM phase is the one yielding the highest relative error on the cell parameter, around 3%. The differences between the FM and AFM-G are less noticeable. With the B3LYP functional, the error on the cell volume is decreased with respect to experimental data.

Råsander *et al.* [5] reported the phonon dispersion curves for the nonmagnetic case, showing that the NM case is structurally unstable, with imaginary phonon energies over the whole first Brillouin zone. In Ref. [4], DFT calculations were performed with the LDA, the PBE, and the PW91 functional, in the non-spin-polarized case and in the spin-polarized case as well. However, they focused on the non-spin-polarized case, which is unstable [5], and our hybrid functional results are in agreement with this observation. In terms of lattice parameters, the NM phase systematically underestimate the lattice parameters. These results highlight that the magnetic structure is important in the case of $FeSb_3$. Comparison with experimental data is also difficult, considering that $FeSb_3$ has never been synthesized in bulk form.

The spin contributions to the magnetic moment are reported in Table II, for both functionals. The magnetic moments are localized in the iron 3d orbitals. With B1WC, the ferromagnetic phase shows an effective magnetic moment per Fe lower than that in the antiferromagnetic phase by 0.31 μ_B with B1WC, and 0.41 μ_B with B3LYP. These results

TABLE II. Optimized magnetic moment per atoms. The asterisk * refers to calculations performed within the $P23$ space group.

	M (μ_B)	FM	AFM-G*
B1WC	Fe	1.29	1.60
	Sb	0.10	0.00
B3LYP	Fe	1.43	1.84
	Sb	0.14	0.00

are higher than what has been observed experimentally with the effective paramagnetic moments of 0.57(6) μ_B in thin films of $FeSb_3$ [2]. Sb remains spin-free in the AFM-G phase, but displays a small spin in the FM phase with an effective moment of -0.09 μ_B. The AFM-G magnetic moment relaxes to 1.60 μ_B/Fe. Isosurfaces of spin density are plotted in Fig. 2 and display d_{z^2} orbital shape, which is a clear indication that crystal field effects due to the distorted octahedra lift the degeneracy on the e_g orbitals, where the d_{z^2} hold the spin.

We calculate the magnetic-coupling constants between first (J_1) and second (J_2) Fe neighbors (when possible in the conventional cell), in the Heisenberg Hamiltonian model,

$$H_{\text{Heisenberg}} = -\sum_{i<j} J_{ij}\, \mathbf{s}_i \cdot \mathbf{s}_j, \tag{8}$$

where i and j are labels on the iron. If we work at fixed AFM-G geometry, we find $J_1 = -3.37$ meV, leading to an estimate of the Néel temperature at $T_N = 109$ K, which is lower than the predicted value of 175 K by Råsander *et al.* [5], but still higher than the experimental $T_N \approx 0$ K. If we add the interaction with second neighbors (possible in the AFM-G unit cell), we find $J_2 = 0.36$ meV and $T_N = 133$ K, the same order of magnitude, showing that second neighbors represent at most 20% of the total exchange strength.

If we properly take into account the relaxation of the atomic structure of the FM phase, and restrict interactions between first neighbors, we find $J_1 = -0.17$ meV and $T_N = 6$ K, now consistent with the experimental data of Möchel *et al.* [2]. This is in contrast with the result from Råsander *et al.* [5], who also take into account structural relaxation. This has to be assigned to the different E_{xc} functional, as highlighted in the previous section, both for the phase ordering and the energy difference. Within B3LYP, the energy difference between the AFM-G and the FM phases is higher, reaching 58 meV. In this case, $J_1 = -4.82$ meV, leading to $T_N = 198$ K, closer to Ref. [5], and failing to predict the paramagnetic phase observed by Möchel *et al.* [2].

Summarizing, our results show that both xc functionals and the relaxation of the crystal structure are crucial to understand the magnetic interactions of $FeSb_3$. Unfortunately, the differences in final atomic positions between the FM and AFM-G phases are probably too small to be detected by XRD. The inclusion of a fraction of HF exact exchange is essential to obtain the AFM-G ground state, but too much (B3LYP) overstabilizes the AFM-G.

B. Electronic structure

As the AFM-G configuration yields the closest results compared to experimental observation, we focus on this magnetic order for the study of the electronic properties. The electronic band structure is plotted for high-symmetry points in the Brillouin zone ($\Gamma \to X \to M \to R \to \Gamma$) in Fig. 3. The band structure presents a small gap of 33 meV, which is close to the reported experimental value [2] of 16.3 meV. In the FM phase, the band structure also displays a small direct band gap of 130 meV. The GGA calculations of Råsander *et al.* produce a ferromagnetic ground state and a "quasi-half-metal," where one spin channel is dominant at the Fermi level [5].

For the NM phase, DFT calculations from Ref. [4] predicted a fully metallic state for the non-spin-polarized configuration, as we do in the hybrid functional formalism. Råsander *et al.* find the same metallic behavior but further show

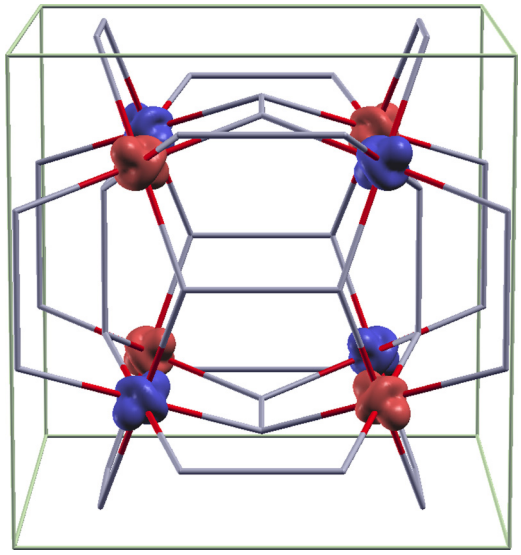

FIG. 2. (Color online) Isosurface of spin density of the AFM-G magnetic phase, with B1WC. The Fe atoms carry the d_{z^2} orbitals, oriented towards the center of the cube [28].

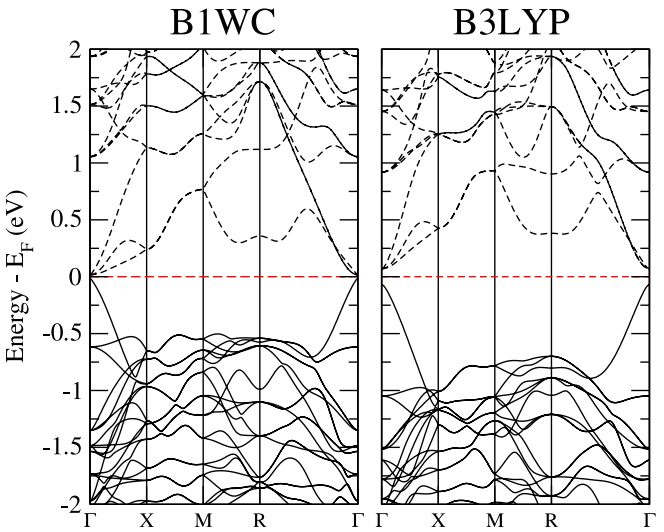

FIG. 3. (Color online) Electronic band structure for the AFM-G phase. The dashed red line is the Fermi level. Empty bands are in black dashed lines.

the configuration to be dynamically unstable, which renders its use in Ref. [4] questionable. We show below that all of the properties (magnetism, semiconducting behavior, and transport) can be explained with the AFM-G model.

Our electron band structures are rather analogous to calculations [29] on $CoSb_3$, where a single band is present below the Fermi level. In our AFM-G band structure, below the gap, a single band disperses strongly around the Γ point, which results in a small density of states, until a strong peak 0.5 eV below E_F. A similar band structure is obtained for the AFM-G phase with the B3LYP functional. The band gap is much larger, equal to 140.8 meV, far from the value calculated with the B1WC functional. Additionally, the density of states has a peak lower in energy, around −0.75 eV. The discrepancies between the B1WC and the B3LYP show that exchange-correlation effects have a nonnegligible impact on the properties of $FeSb_3$. There is a competition between the volume and the exchange-correlation effects on the band gap, which explains the decrease of the gap despite a smaller volume with the B1WC functional, which uses less HF exchange than B3LYP. The effect of HF exchange has been investigated by computing self-consistently the electronic structure for the AFM-G and FM phase, at fixed optimized B1WC geometry, by changing only the percentage of HF exchange in the B1WC functional, keeping all the other parameters the same. It is found that between 13% and 18% of HF exchange, the stability of one phase versus the other becomes ambiguous, which is consistent with the paramagnetic phase observed by Möchel and coworkers [2].

Our B1WC hybrid functional results are fully consistent with experiments, and show that the exchange-correlation effects are crucial to obtain the correct ground state, magnetism, and electronic band gap. As the B1WC predicts more accurately the band gap, the analysis of the transport properties will focus on the B1WC band structure.

Slightly above the conduction band minimum, the DOS increases, which suggests that the transport properties may be enhanced via *n*-type doping. This will be analyzed in the following section.

The charge carrier density obtained from the Hall effect measurement on a 1.5 μm thick $FeSb_3$ sample is shown in Fig. 4. The noise at close to room temperature is larger, and attributed partly to the silver paint contacts. The charge carrier density is essentially constant at $4(1) \times 10^{19}$ cm^{-3} below 180 K, then increases gradually and reaches $3(1) \times 10^{20}$ cm^{-3} at room temperature. This sudden increase of charge carrier density might be associated with thermal excitation of defects. The sign of the Hall voltage indicates *p*-type conductivity. We will now quantify the relation between $1/R_H$ and the true carrier density.

The comparison of transport data with experimental data is complicated by the diversity of the samples and reported carrier densities. The formula $n_h = \frac{1}{(eR_H)}$, often used to extract carrier densities, is derived from a free-electron model and is not valid in case of nonparabolic bands. In Fig. 3, doping values above 10^{20} cm^{-3} shift the chemical potential into a region where the band structure is no longer parabolic. In Fig. 5 we compare the value of R_H derived from our Boltzmann transport theory calculation with the value obtained from the aforementioned formula. The errors are around 1%

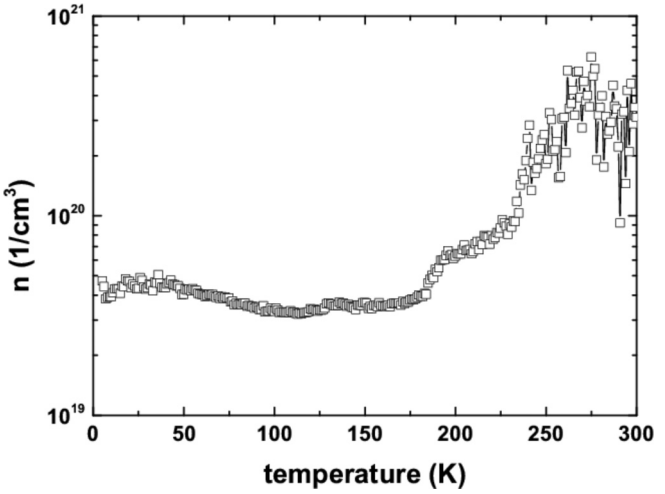

FIG. 4. The charge carrier concentration as function of temperate in $FeSb_3$.

for $n_h \approx 10^{19}$ cm^{-3} from 0 K to 300 K but grow rapidly for larger concentrations. The range where the error is less than 20%, only goes up to 1.2×10^{21} cm^{-3} hole density. The invalidity of the parabolic band model for the higher carrier densities implies an overestimation of the hole density in Ref. [4], where the combination of a metallic NM band structure and large apparent carrier density (10^{22} cm^{-3}) leads to calculated *S* in agreement with experiment. In our AFM-G semiconducting case, we will show below agreement for the Seebeck coefficient with lower effective carrier densities.

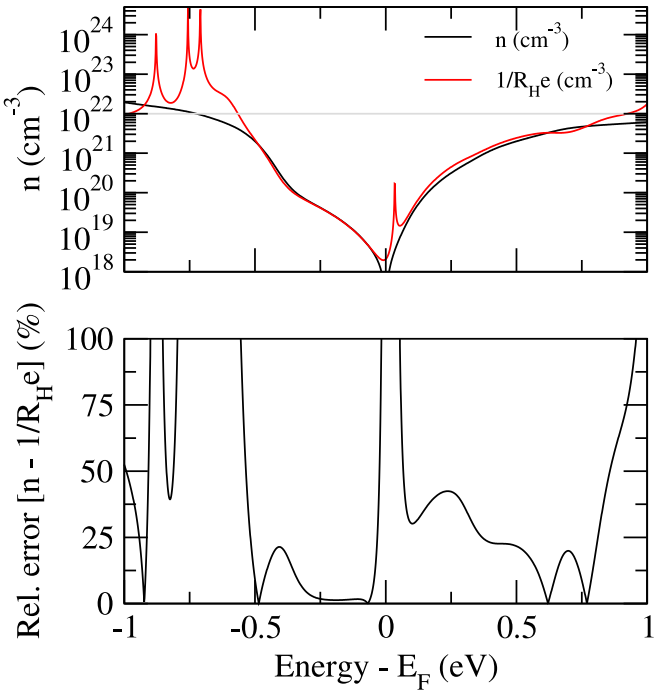

FIG. 5. (Color online) Carrier densities as computed from the density of states, and the relative error with respect to the $1/eR_H$ formula, at 300 K, where R_H is computed from Boltzmann theory. The horizontal line in the top plot indicates $n_h = 10^{22}$ cm^{-3}.

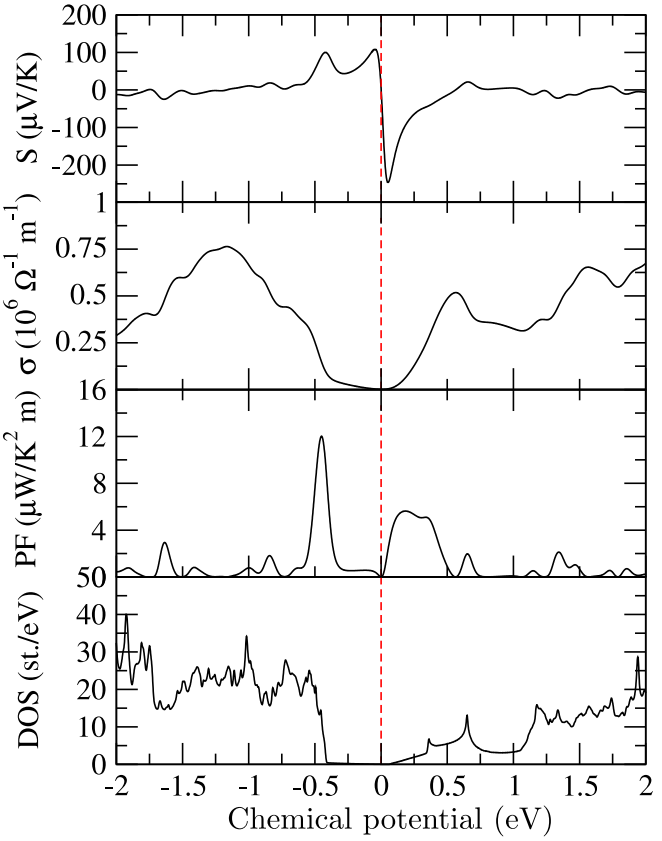

FIG. 6. (Color online) Seebeck coefficient, electrical conductivity over τ, and power factor (with $\tau = 5.5 \times 10^{-15}$ s) of AFM-G $FeSb_3$ with respect to the chemical potential, at 300 K. The electronic density of states computed with the B1WC functional is also displayed for direct comparison.

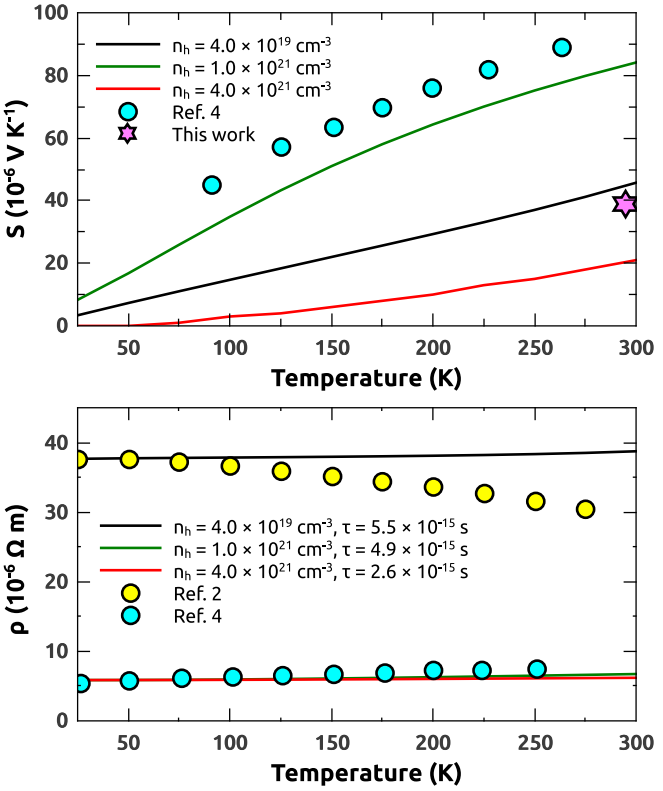

FIG. 7. (Color online) Seebeck coefficient and electrical conductivity evolution of AFM-G $FeSb_3$ with respect to temperature, for fixed hole concentrations and fixed lifetime. Experimental measurements from this work and Refs. [2] and [4] are given for comparison.

C. Thermoelectric properties

The thermoelectric and transport properties are computed from the B1WC electronic band structure within the Boltzmann transport theory. We plot S, σ/τ, and the power factor $S^2\sigma$ as a function of the chemical potential, at 300 K (Fig. 6), and with respect to temperature for fixed charge carrier concentrations (Fig. 7).

From these plots, we can see that a light n-type doping enhances the thermopower. However, the large peak around 0.5 eV below the Fermi level shows that p-type doping will maximize $S^2\sigma$ (12 μW K^{-2} cm^{-1}) with a concentration of charge carriers of about 8.4×10^{20} cm^{-3}. This corresponds to a strong doping. For n-type doping, the maximum power factor (5 μW K^{-2} cm^{-1}) at 300 K is obtained for doping of 1.5×10^{20} cm^{-3}. One may expect the n-type to be the easier option to reach the high power factor, but a similar value can be reached for a p-type doping of 2.3×10^{20} cm^{-3}. The peak of power factor in the hole carrier region is due to an increase of the Seebeck coefficient, related to the presence of new states below the topmost valence band.

Figure 7 shows the temperature dependence of the Seebeck coefficient (top). The black, red, and green curves are obtained by fixing the hole density respectively to 4.0×10^{19} cm^{-3}, 1.0×10^{21} cm^{-3}, and 4.0×10^{21} cm^{-3} to get the same order of magnitude as the carrier density extracted from Fig. 4. The Seebeck coefficient has a monotonic growth. Experimental results from Ref. [4] and our room temperature measurement are also displayed in Fig. 7 for comparison. Our calculated values underestimate the Seebeck coefficient in comparison to these data, but the qualitative behavior is consistent. Daniel *et al.* [4] reported a high value of hole density, above 10^{22} cm^{-3} for the corresponding sample.

The Seebeck coefficient, as measured with the Seebeck microprobe on an area of 4×3mm^2 of the thin-film sample, is displayed in Fig. 8. The distribution in Seebeck coefficient is relatively uniform and narrow with a half-width of 1.5 μV K^{-1}, and a mean value of 38.6 μV K^{-1}, which is consistent with the predicted value at 300 K for $n_h = 4.0 \times 10^{19}$ cm^{-3} given the expected underestimation with the Seebeck local probe technique. This suggests that the effective carrier concentration near the surface is lower than in the bulk, but may also come from the shortcomings of DFT, or the relaxation time approximation.

In order to have a quantitative appreciation of the electrical resistivity ρ, it is necessary to calculate the relaxation time τ for different temperatures and carrier densities. A common way to estimate τ is to perform the ratio between computed σ/τ and the experimental value, at the corresponding doping level. However, this task is tricky because the available experimental data on σ are scarce; moreover, the associated carrier densities are quite different. The reader shall keep in mind that these values are only used to simplify the comparison between our results and the available experimental data. The resistivity can

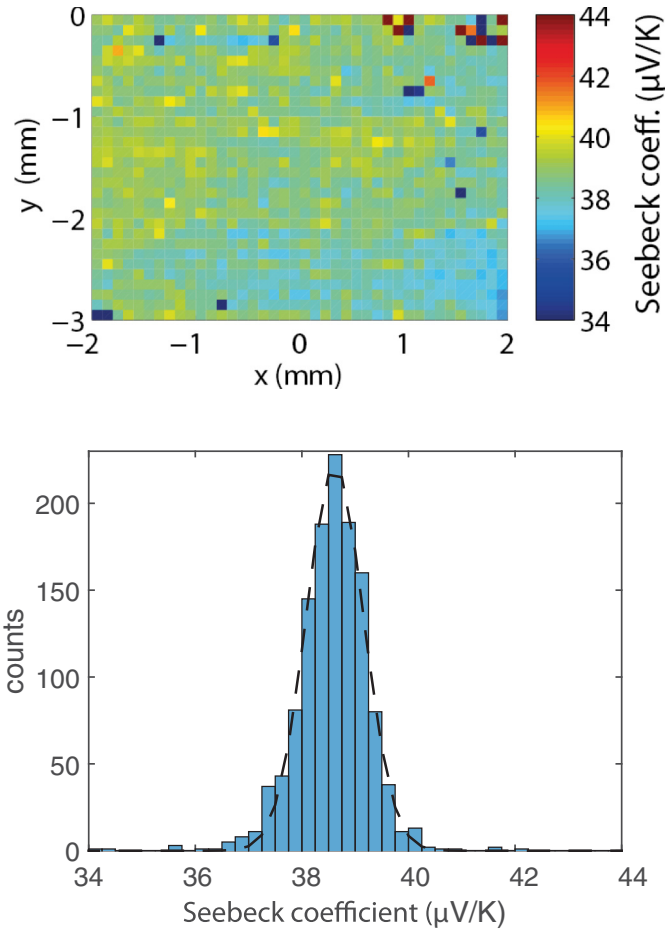

FIG. 8. (Color online) The Seebeck coefficient map (up), where x and y are coordinates, and its distribution (down) on a representative area of a $FeSb_3$ film at room temperature.

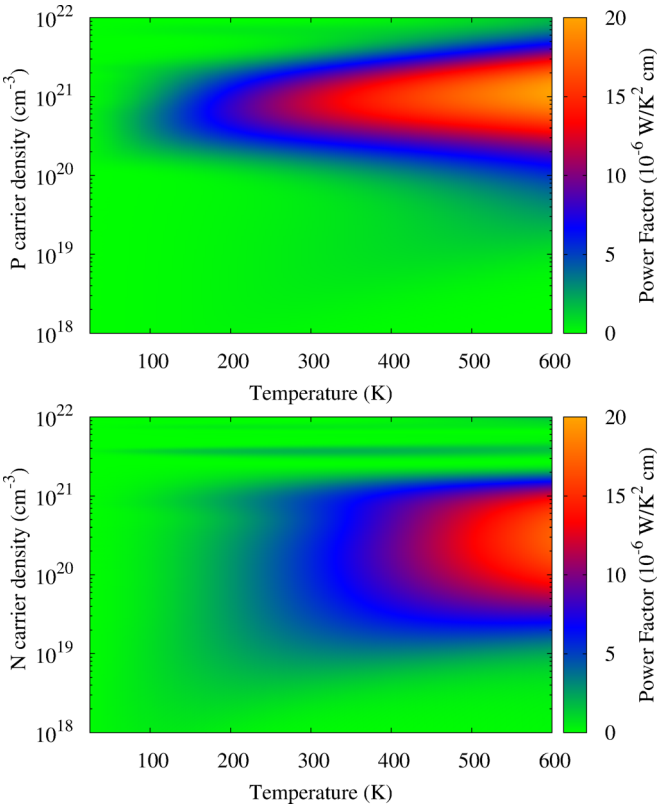

FIG. 9. (Color online) Power factor map with respect to temperature and doping. The relaxation time was fixed to 5.5×10^{-15} s.

be compared with the measurements of Möchel *et al.* [2] and those of Daniel *et al.* [4]. The black, red, and green curves are obtained by fixing the hole concentration respectively, in the same fashion as we did for the Seebeck coefficient. The relaxation time for the black curve was estimated by fitting the resistivity to the value reported by Möchel *et al.* [2] whereas the red and green curves were fitted. Our calculated values of ρ all increase with the temperature, in contrast to the experiment of Möchel *et al.* There is a competition between the increase in charge carriers (Fig. 4), which lowers ρ, and the increase of the scattering rate at high temperature, which increases ρ. In the specific case of $FeSb_3$, the first effect is dominant, and our results are in agreement with the experiment: increasing the carrier density leads to a much lower resistivity. Yet, these results have been obtained for a constant relaxation time. A more realistic prediction, more accurate with the results of Möchel *et al.*, may be obtained by taking into account the effect of scattering at high temperature, which tends to decrease the relaxation time, competing with the increase of charge carriers, resulting in a less drastic drop of resistivity. Recent experimental studies [4] have highlighted a different behavior of the resistivity (Fig. 7, bottom), which display a metallic behavior, which is more consistent with our theoretical results. However, the order of magnitude is roughly five times less than what was measured from films by Möchel *et al.* [2]. The calculated Seebeck coefficient and electrical resistivity, for a carrier density of 10^{21} cm^{-3}, match the results from Ref. [4] obtained on samples with a doping of 10^{22} cm^{-3}. At our level of calculation, for a doping of carrier density of 4×10^{21} cm^{-3}, the Seebeck coefficient no longer matches the experimental results. There are several reasons for this; first, we study $FeSb_3$ in its bulk form, neglecting surface effects, while experimental studies were performed on thick films. Moreover, the system has been synthesized on different substrates, which may explain the differences between the reported cell parameters. Additionally, above dopings of 10^{21} cm^{-3}, the rigid-band approximation may become spurious, leading to a different energy landscape and, ultimately, different thermoelectric properties.

One question remains: can $FeSb_3$ be a good thermoelectric? Figure 9 shows the evolution of the power factor with respect to carrier densities, for a p-type and n-type doping. As observed previously, p-type doping is the better strategy to optimize the power factor over a wide range of temperature, for doping value around 10^{21} cm^{-1}. At room temperature, the power factor reaches 12 μW/K^2 cm, which is lower than the maximum room temperature power factor of unfilled CoSb3 (30 μW/K^2 cm), obtained with optimal p-type or n-type doping [30]. However, the power factor goes up to 20 μW/K^2 cm at higher temperatures (600 K). On the other hand, n-type doping is not as efficient, but nonetheless manages to improves the power factor up to 14 μW/K^2 cm from 500 to 600 K.

IV. CONCLUSIONS

We combine local probe Seebeck experiments with first-principles calculations to dissect the electronic, magnetic, and transport properties of the unfilled skutterudite $FeSb_3$. Using a hybrid functional formalism, we model the exchange-correlation energy and compute the structural, magnetic, electronic, and thermoelectric properties. One nonmagnetic phase and two magnetic phases are relaxed. We find that the ground state is the AFM-G phase, but the differences in total energy and in structural properties with the FM phase are slight. This is consistent with the compound being paramagnetic at finite temperature, in agreement with previous experiments [2]. The electronic band structure of $FeSb_3$ behaves similarly to $CoSb_3$, with a small density of states in the top 0.5 eV of the valence band, due to the dispersion of a single band around the Γ point. There is a small band gap of 33 meV with B1WC, and 140.8 meV with B3LYP. The thermoelectric properties were obtained from the electronic structure using Boltzmann transport theory: the temperature dependence of the Seebeck coefficient, the electrical conductivity, and the related power factor are computed. Different behaviors (semiconductor, metallic) are obtained depending on the doping. Results between B1WC and B3LYP differ slightly: the former gives a better prediction of the band gap, but yields a smaller volume; the latter gives a much larger band gap, but the volume is more accurate with respect to experimental data. Comparison of our electrical resistivity in bulk $FeSb_3$ with the experiments on thin films performed by Möchel *et al.* [2] suggests a multivalent defect as the source of the additional carriers at higher temperature. However, the qualitative behavior of the resistivity with respect to temperature matches the experiments from Ref. [4]. We measure a Seebeck coefficient of 38.6 μV K^{-1} at room temperature, which is consistent with calculated values for intermediate carrier concentrations, and a lower surface carrier density. Our theoretical TE properties are consistent with experimental studies from Daniel *et al.* The discrepancies between experimental studies may point to different properties of the surface from the bulk. Boltzmann transport analysis has been performed in the relaxation time approximation [4]; however the thermoelectric properties have been computed from a different band structure, not taking into account the magnetization of the compound, which has been demonstrated to be critical. Moreover, the excess of Sb atoms leads to *n*-type doping, which should leads to a negative Seebeck coefficient and a negative Hall resistance as well. However, their hole concentration results does not match the Sb doping, which is important enough at 300 K ($> 10^{22}$ cm^{-3}) to change the sign of the majority carriers. We show that the traditional semiclassical model to extract carrier densities overestimates the hole concentration, which may be an explanation for this discrepancy. The power factor can be significantly enhanced with experimentally accessible values of *n*-type and *p*-type doping.

ACKNOWLEDGMENTS

J.d.B. would like to thank the Helmholtz Association for endorsement. Work partially supported by DFG SPP1386 "Nanostructured Thermoelectrics" (B.K.) and by the US Department of Energy, Office of Science, Basic Energy Sciences, Materials Sciences and Engineering Division (R.P.H.). We acknowledge an ARC grant (TheMoTherm 10/15-03) from the Communauté Française de Belgique. Computer time was made available by PRACE-2IP and 3IP on Hector and Archer (EU FP7 Grants No. RI-283493 and No. RI-312763), CECI, and SEGI-ULg.

[1] K. Momma and F. Izumi, J. Appl. Crystallogr. **44**, 1272 (2011).
[2] A. Möchel, I. Sergueev, N. Nguyen, G. J. Long, F. Grandjean, D. C. Johnson, and R. P. Hermann, Phys. Rev. B **84**, 064302 (2011).
[3] M. D. Hornbostel, E. J. Hyer, J. Thiel, and D. C. Johnson, J. Am. Chem. Soc. **119**, 2665 (1997).
[4] M. V. Daniel, L. Hammerschmidt, C. Schmidt, F. Timmermann, J. Franke, N. Johrmann, M. Hietschold, D. C. Johnson, B. Paulus, and M. Albrecht, Phys. Rev. B **91**, 085410 (2015).
[5] M. Råsander, L. Bergqvist, and A. Delin, Phys. Rev. B **91**, 014303 (2015).
[6] G. Xing, X. Fan, W. Zheng, Y. Ma, H. Shi, and D. J. Singh, Sci. Rep. **5**, 10782 (2015).
[7] R. Dovesi, R. Orlando, B. Civalleri, C. Roetti, V. R. Saunders, and C. M. Zicovich-Wilso, Z. Kristallogr. **220**, 571 (2005).
[8] W. Kohn and L. J. Sham, Phys. Rev. **140**, A1133 (1965).
[9] M. Catti, G. Valerio, and R. Dovesi, Phys. Rev. B **51**, 7441 (1995).
[10] M. Causa, R. Dovesi, and C. Roetti, Phys. Rev. B **43**, 11937 (1991).
[11] S. H. Vosko, L. Wilk, and M. Nusair, Can. J. Phys. **58**, 1200 (1980).
[12] D. I. Bilc, R. Orlando, R. Shaltaf, G. M. Rignanese, J. Iniguez, and P. Ghosez, Phys. Rev. B **77**, 165107 (2008).
[13] A. D. Becke, Phys. Rev. A **38**, 3098 (1988).
[14] Z. Wu and R. E. Cohen, Phys. Rev. B **73**, 235116 (2006).
[15] A. D. Becke, J. Chem. Phys. **98**, 5648 (1993).
[16] R. Demichelis, B. Civalleri, P. D'Arco, and R. Dovesi, Int. J. Quantum Chem. **110**, 2260 (2010).
[17] R. Demichelis, B. Civalleri, M. Ferrabone, and R. Dovesi, Int. J. Quantum Chem. **110**, 406 (2010).
[18] J. Varignon and P. Ghosez, Phys. Rev. B **87**, 140403 (2013).
[19] N. C. Bristowe, J. Varignon, D. Fontaine, E. Bousquet, and P. Ghosez, Nat. Commun. **6**, 6677 (2015).
[20] M. Reinle-Schmitt, C. Cancellieri, D. L. D. Fontaine, M. Medarde, E. Pomjakushina, C. Schneider, S. Gariglio, P. Ghosez, J.-M. Triscone, and P. Willmott, Nat. Commun. **3**, 932 (2012).
[21] D. I. Bilc and P. Ghosez, Phys. Rev. B **83**, 205204 (2011).
[22] D. I. Bilc, G. Hautier, D. Waroquiers, G.-M. Rignanese, and P. Ghosez, Phys. Rev. Lett. **114**, 136601 (2015).
[23] H. J. Monkhorst and J. D. Pack, Phys. Rev. B **13**, 5188 (1976).

[24] G. Madsen and D. Singh, Comput. Phys. Commun. **175**, 67 (2006).

[25] D. Platzek, G. Karpinski, C. Stiewe, P. Ziolkowski, C. Drasar, and E. Muller, in *24th International Conference on Thermoelectrics (ICT): Clemson, SC, 19-23 June 2005* (IEEE, Piscataway, NJ, 2005), p. 13.

[26] P. Ziolkowski, G. Karpinski, T. Dasgupta, and E. Müller, Phys. Status Solidi (a) Appl. Mater. Sci. **210**, 89 (2013).

[27] L. van der Pauw, A Method of Measuring Specific Resistivity and Hall Effect of Discs of Arbitrary Shape, Philips Research Reports **13**, 1 (1958).

[28] A. Kokalj, Comput. Mater. Sci. **28**, 155 (2003).

[29] M. Veithen and P. Ghosez, J. Phys.: Condens. Matter **19**, 096002 (2007).

[30] T. Caillat, A. Borshchevsky, and J. Fleurial, J. Appl. Phys. **80**, 4442 (1996).